Universal current correlations induced by the Majorana and fermionic Andreev bound states

Kunhua Zhang,[1,2] Xinlong Dong,[3,1] Junjie Zeng,[1,2] Yulei Han,[1,2] and Zhenhua Qiao[1,2,*]

[1]*ICQD, Hefei National Laboratory for Physical Sciences at Microscale, and Synergetic Innovation Center of Quantum Information and Quantum Physics, University of Science and Technology of China, Hefei, Anhui 230026, China*

[2]*CAS Key Laboratory of Strongly-Coupled Quantum Matter Physics, and Department of Physics, University of Science and Technology of China, Hefei, Anhui 230026, China*

[3]*College of Physics and Information Engineering, and Research Institute of Materials Science, Shanxi Normal University, Linfen, Shanxi 041004, China*

(Received 3 June 2018; published 25 July 2019)

Majorana bound states have been proposed to induce current-current correlations (CCCs) that are completely different from those induced by low-energy fermionic Andreev bound states. Such characteristics can be used as a signature to detect Majorana bound states and their nonlocality. Herein, we studied the Majorana and fermionic Andreev bound states in a two-dimensional topological insulator system. We found that the coupling of each pair of fermionic Andreev bound states coexists with that of the pair of Majorana bound states, and that the coupling strengths of all pairs of bound states depend on system parameters in the same pattern. Majorana and fermionic Andreev bound states show the same differential CCCs characteristics, thereby indicating a universal behavior for both types of bound states in a two-dimensional topological insulator system. The maximal cross-differential CCCs are robust to the structural asymmetry of the system.

DOI: 10.1103/PhysRevB.100.045421

I. INTRODUCTION

In condensed matter systems, Majorana bound states (MBSs) are exotic excitations of zero energy [1,2], which provide an attractive platform for topological quantum computation [3–6]. Among various condensed matter systems, topological superconductors represent a natural means of searching MBSs and therefore have recently attracted considerable attention [7–9]. A variety of candidate topological superconductor systems have been proposed [10–16], and multiple studies have been conducted to verify the existence of MBSs in them [17–25]. Through experiments, some evidence has been found for the existence of MBSs owing to phenomena such as resonant Andreev reflection, fractional Josephson effect, selective equal-spin Andreev reflection, and half-integer conductance plateau [26–32]. However, because these phenomena have possible physical explanations, except for MBSs, more compelling experimental evidence regarding these signatures is required to settle the debate on MBSs [33–38].

A characteristic of MBSs is their nonlocality. It can be probed by the nonlocal transport if there is coupling between MBSs. The coupling comprises Coulomb coupling and tunnel coupling [39–43]. Herein, we study crossed Andreev reflection for the case of tunnel coupling [19,44,45]. When MBSs are tunnel coupled, local Andreev reflection is predicted to be completely suppressed at sufficiently low excitation energy while favoring crossed Andreev reflection. A characteristic of this enhanced crossed Andreev reflection is maximal cross current-current correlation (CCC) [40].

Moreover, previous studies have shown that the CCCs induced by MBSs differ from those induced by ordinary low-energy fermionic Andreev bound states (ABSs) in superconducting semiconductor nanowires and Fe chains [46,47]. Therefore, a question arises as to whether the maximal cross CCC is unique to MBSs, which is crucial to distinguish MBSs from fermionic ABSs. This fundamental question motivates us to move beyond the superconducting semiconductor nanowires and Fe chains, and to explore further the CCCs induced by MBSs and fermionic ABSs in a two-dimensional topological insulator (2D TI) system. We found that the coupling of each pair of fermionic ABSs coexists with that of the pair of MBSs, and that the coupling strengths of all pairs of bound states display the same tendency with the changes of the system parameters. These bound states result in the same maximal cross-differential CCCs. Such correlations are robust and universal in our setup. These intriguing properties of both types of bound states in 2D TI systems make a significant step toward understanding the properties of MBSs and fermionic ABSs. In order to definitely differentiate MBSs from fermionic ABSs in 2D TI systems, it is therefore necessary to have signatures beyond the CCCs.

The rest of this paper is as follows. Section II describes the model under study and gives the formalism. Sections III and IV present the results on the MBSs and fermionic ABSs, on the current-current correlations, and the related discussions. Section V concludes this paper. Some auxiliary materials are given in the Appendices.

II. MODEL AND FORMALISM

We consider MBSs and ordinary fermionic ABSs in one-dimensional ferromagnetic-insulator–edge-state–superconductor (FI–ES–SC) junction systems mediated on

*Corresponding author: qiao@ustc.edu.cn

 ©2019 American Physical Society

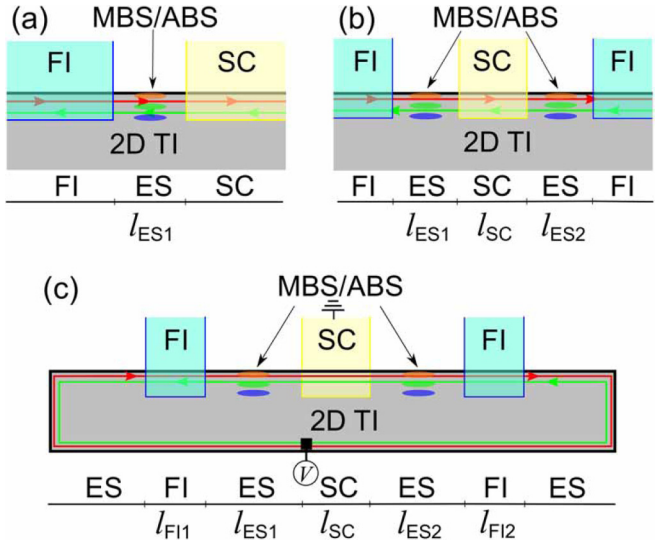

FIG. 1. Schematics of one-dimensional ferromagnetic-insulator–edge-state–superconductor (FI–ES–SC) junctions mediated by the ESs of a two-dimensional topological insulator (2D TI): (a) FI–ES–SC junction; (b) FI–ES–SC–ES–FI junction; (c) ES–FI–ES–SC–ES–FI–ES junction.

the edge of a 2D TI, as shown in Fig. 1. The ferromagnetism and superconductivity of the ESs are induced by the proximity effects of the FI and the s-wave SC, respectively, which interact with the electrons in the ESs of a 2D TI [11].

The one-dimensional junctions can be described by the following Bogoliubov–de Gennes equation [11,40]:

$$\begin{pmatrix} \upsilon_F \sigma_x p_x + \boldsymbol{\sigma}\cdot\boldsymbol{m} - \mu & \Delta e^{i\phi} \\ \Delta e^{-i\phi} & -\upsilon_F \sigma_x p_x + \boldsymbol{\sigma}\cdot\boldsymbol{m} + \mu \end{pmatrix} \psi = E\psi, \tag{1}$$

where $\boldsymbol{\sigma} = (\sigma_x, \sigma_y, \sigma_z)$, υ_F, ψ, and E are the Pauli matrices, Fermi velocity, wave function, and excitation energy, respectively. $\Delta e^{i\phi}$ denotes the superconducting pair potential, where Δ and ϕ are the energy gap and the phase, respectively. Because ϕ makes no difference to the calculations, we set it to be zero. The chemical potential or Fermi energy $\mu(x)$ is position dependent and could cross the different positions of the energy band. $\mu(x)$ is measured with respect to the Dirac point, which can be tuned via the gate voltage or doping independently in each region. In the following, μ_{ES1} and μ_{ES2} denote the chemical potentials at the left and right ESs around the SC, respectively. The chemical potentials for the SC and the left and right FIs are represented by μ_{SC}, μ_{FI1}, and μ_{FI2}, respectively. In Fig. 1(a), the magnetization is $\boldsymbol{m}(x) = (m_{lx}, m_{ly}, m_{lz})$ for $x < -l_{ES1}$ and $\boldsymbol{m}(x) = 0$ otherwise. In Fig. 1(b), the magnetization is set as $\boldsymbol{m}(x) = (m_{lx}, m_{ly}, m_{lz})$ for $x < -l_{ES1}$ and $\boldsymbol{m}(x) = (m_{rx}, m_{ry}, m_{rz})$ for $x > l_{SC} + l_{ES2}$. By solving Eq. (1), we obtain the wave functions for the junctions shown in Figs. 1(a) and 1(b).

The wave function of the left FI in Fig. 1(a) is obtained as follows:

$$\psi_{FI1} = a_e \psi^e_{FI1} \exp\left[-i\left(k_l + \frac{2m_{lx}}{\hbar\upsilon_F}\right)x\right] + a_h \psi^h_{FI1} \exp\left[i\left(\frac{2m_{lx}}{\hbar\upsilon_F} - k'_l\right)x\right], \tag{2}$$

where $\psi^e_{FI1} = (-\hbar\upsilon_F k_l - m_{lx} - im_{ly}, E + \mu_{FI1} - m_{lz}, 0, 0)^T$ and $\psi^h_{FI1} = (0, 0, \hbar\upsilon_F k'_l - m_{lx} - im_{ly}, E - \mu_{FI1} - m_{lz})^T$. T indicates matrix transposition. $k_l = (i\sqrt{-(E + \mu_{FI1})^2 + m^2_{lz} + m^2_{ly}} - m_{lx})/\hbar\upsilon_F$ and $k'_l = (i\sqrt{-(E - \mu_{FI1})^2 + m^2_{lz} + m^2_{ly}} + m_{lx})/\hbar\upsilon_F$. a_e and a_h are the coefficients of the electron and hole wave functions, respectively.

The ES wave function is obtained as follows:

$$\psi_{ES1} = b_e \psi^e_{ES1} \exp(ik_1 x) + b'_e \psi^{e'}_{ES1} \exp(-ik_1 x) + c_h \psi^h_{ES1} \exp(ik_2 x) + c'_h \psi^{h'}_{ES1} \exp(-ik_2 x), \tag{3}$$

where b_e, b'_e, c_h, and c'_h are the coefficients of wave functions. $\psi^e_{ES1} = (\hbar\upsilon_F k_1, E + \mu_{ES1}, 0, 0)^T$, $\psi^{e'}_{ES1} = (-\hbar\upsilon_F k_1, E + \mu_{ES1}, 0, 0)^T$, $\psi^h_{ES1} = (0, 0, -\hbar\upsilon_F k_2, E - \mu_{ES1})^T$, and $\psi^{h'}_{ES1} = (0, 0, \hbar\upsilon_F k_2, E - \mu_{ES1})^T$. Here, $k_1 = (\mu_{ES1} + E)/\hbar\upsilon_F$, and $k_2 = (\mu_{ES1} - E)/\hbar\upsilon_F$.

The SC wave function is obtained as follows:

$$\psi_{SC} = d\psi'_{SC} \exp[(-\kappa - ik_{SC})x] + f\psi''_{SC} \exp[(-\kappa + ik_{SC})x], \tag{4}$$

where $\psi'_{SC} = (-\exp[i(\phi - \alpha)], \exp[i(\phi - \alpha)], -1, 1)^T$, $\psi''_{SC} = (\exp[i(\phi + \alpha)], \exp[i(\phi + \alpha)], 1, 1)^T$, $k_{SC} = \mu_{SC}/\hbar\upsilon_F$, $\alpha = \arccos(E/\Delta)$ for $E < \Delta$, and $\kappa = \Delta \sin\alpha/\hbar\upsilon_F$. d and f are coefficients of wave functions that are coherent superpositions of the electron and hole excitations. The wave functions in different regions satisfy continuity conditions at the interfaces $\psi_{FI1}(x = -l_{ES1}) = \psi_{ES1}(x = -l_{ES1})$ and $\psi_{ES1}(x = 0) = \psi_{SC}(x = 0)$, which determine the properties of the bound states.

With the same method, we can obtain the wave functions for junction in Fig. 1(b). The wave functions of the left FI, left ES in Fig. 1(b) are ψ_{FI1} and ψ_{ES1}, respectively, which are the same as those in Fig. 1(a). However, the SC wave function is now obtained as follows:

$$\psi_{SC} = d\psi'_{SC} \exp[(-\kappa - ik_{SC})x] + f\psi''_{SC} \exp[(-\kappa + ik_{SC})x] + d'\psi'''_{SC} \exp[(\kappa + ik_{SC})x] + f'\psi''''_{SC} \exp[(\kappa - ik_{SC})x], \tag{5}$$

where $\psi'''_{SC} = (\exp[i(\phi - \alpha)], \exp[i(\phi - \alpha)], 1, 1)^T$ and $\psi''''_{SC} = (-\exp[i(\phi + \alpha)], \exp[i(\phi + \alpha)], -1, 1)^T$. d, d', f, and f' are coefficients of wave functions that are coherent superpositions of the electron and hole excitations.

The right ES wave function is obtained as follows:

$$\psi_{ES2} = g_e \psi^e_{ES2} \exp(ik_3 x) + g'_e \psi^{e'}_{ES2} \exp(-ik_3 x) + p_h \psi^h_{ES2} \exp(ik_4 x) + p'_h \psi^{h'}_{ES2} \exp(-ik_4 x), \tag{6}$$

where g_e, g'_e, p_h, and p'_h are the coefficients of wave functions. $\psi^e_{ES2} = (\hbar\upsilon_F k_3, E + \mu_{ES2}, 0, 0)^T$, $\psi^{e'}_{ES2} = (-\hbar\upsilon_F k_3, E + \mu_{ES2}, 0, 0)^T$, $\psi^h_{ES2} = (0, 0, -\hbar\upsilon_F k_4, E - \mu_{ES2})^T$, and $\psi^{h'}_{ES2} = (0, 0, \hbar\upsilon_F k_4, E - \mu_{ES2})^T$. Here, $k_3 = (\mu_{ES2} + E)/\hbar\upsilon_F$ and $k_4 = (\mu_{ES2} - E)/\hbar\upsilon_F$.

The wave function of the right FI is obtained as follows:

$$\psi_{FI2} = q_e \psi^e_{FI2} \exp[ik_r x] + q_h \psi^h_{FI2} \exp[ik'_r x], \tag{7}$$

where $\psi^e_{FI2} = (\hbar\upsilon_F k_r + m_{rx} - im_{ry}, E + \mu_{FI2} - m_{rz}, 0, 0)^T$ and $\psi^h_{FI2} = (0, 0, -\hbar\upsilon_F k'_r + m_{rx} - im_{ry}, E - \mu_{FI2} - m_{rz})^T$.

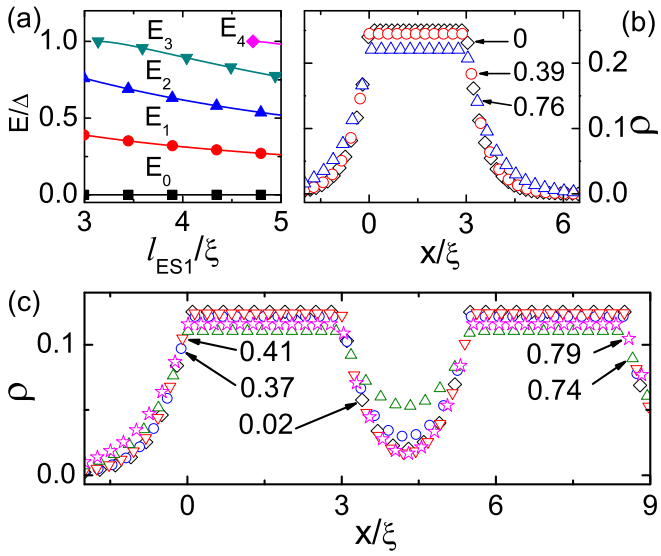

FIG. 2. (a) Energies E of the bound states as function of the ES width l_{ES1} of the FI–ES–SC junction. (b) Probability densities ρ of MBS and ordinary ABSs as functions of x in the FI–ES–SC junction, where $x = 0$ is the interface between the leftmost FI and ES, and the ES width is $l_{\mathrm{ES1}} = 3\xi$. (c) Probability densities ρ of coupled MBS and coupled fermionic ABSs as functions of x in the the FI–ES–SC–ES–FI junction, where $x = 0$ is the interface between the leftmost FI and left ES, where $l_{\mathrm{SC}} = 2.5\xi$, , $l_{\mathrm{ES1}} = l_{\mathrm{ES2}} = 3\xi$. Here, the chemical potential $\mu_{\mathrm{SC}} = 50\Delta$, and $\xi = \hbar\upsilon_{\mathrm{F}}/\Delta$ is the coherence length.

$k_r = (i\sqrt{-(E + \mu_{\mathrm{FI2}})^2 + m_{rz}^2 + m_{ry}^2} - m_{rx})/\hbar\upsilon_{\mathrm{F}}$ and $k_r' = (i\sqrt{-(E - \mu_{\mathrm{FI2}})^2 + m_{rz}^2 + m_{ry}^2} + m_{rx})/\hbar\upsilon_{\mathrm{F}}$. q_e and q_h are the coefficients of the electron and hole wave functions, respectively.

The wave functions in different regions satisfy continuity conditions at the interfaces $\psi_{\mathrm{FI1}}(x = -l_{\mathrm{ES1}}) = \psi_{\mathrm{ES1}}(x = -l_{\mathrm{ES1}})$, $\psi_{\mathrm{ES1}}(x = 0) = \psi_{\mathrm{SC}}^{\backslash}(x = 0)$, $\psi_{\mathrm{SC}}^{\backslash}(x = l_{\mathrm{SC}}) = \psi_{\mathrm{ES2}}(x = l_{\mathrm{SC}})$, and $\psi_{\mathrm{ES2}}(x = l_{\mathrm{SC}} + l_{\mathrm{ES2}}) = \psi_{\mathrm{FI2}}(x = l_{\mathrm{SC}} + l_{\mathrm{ES2}})$, which determine the properties of the bound states in Fig. 1(b).

III. MBSs AND FERMIONIC ABSs

First, we study the MBSs and non-zero-energy fermionic ABSs in the junction shown in Fig. 1(a). Because the electron spin is locked with the momentum of ESs in the 2D TI, both the magnetization and s-wave superconducting pair potential can open gaps in the gapless ESs. As shown in Fig. 1(a), if the FI and SC are infinitely long, bound states can exist in this junction. Based on the wave functions and boundary conditions, the energies E and probability densities ρ of all bound states can be calculated. As shown in Fig. 2(a), the number of bound states increases discontinuously with an increase in the width l_{ES1} of the junction. The zero-energy bound state (i.e., MBS) always exists and is independent of l_{ES1}, whereas the energies of the non-zero-energy bound states (i.e., ordinary fermionic ABSs) decrease with an increase in l_{ES1}.

Figure 2(b) shows the probability densities ρ of the three bound states as functions of the junction position x. The position $x = 0$ represents the interface between the leftmost FI and the ESs, while the position $x = 3\xi$ represents the interface between the ESs and the rightmost SC. The black, red, and blue lines denote the probability densities ρ for these three states with the energies $E/\Delta = 0$, 0.390, and 0.760, respectively. Because the maximal probability densities are in the range $0 < x < 3\xi$, the bound states are localized mainly in the ES region. By comparing the probability densities ρ of the aforementioned three states, we find that the MBS is slightly more localized than the fermionic ABSs.

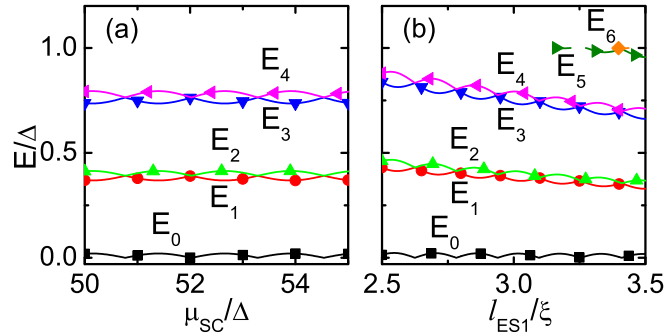

FIG. 3. (a), (b) Energies E of the bound states as functions of the chemical potential μ_{SC} of the SC and the width l_{ES1} of the leftmost ES in the FI–ES–SC–ES–FI junction. Here, the width l_{SC} of the SC is 2.5ξ. (a) $l_{\mathrm{SC}} = 2.5\xi$ and $l_{\mathrm{ES1}} = l_{\mathrm{ES2}} = 3\xi$. (b) $\mu_{\mathrm{SC}} = 50\Delta$ and $l_{\mathrm{ES1}} = l_{\mathrm{ES2}}$.

While coupling another SC–ES–FI junction to the right-hand side of Fig. 1(a), we create an FI–ES–SC–ES–FI junction, as shown in Fig. 1(b). If the width l_{SC} of the SC is sufficiently large, each energy E corresponds to two degenerate bound states, which are localized mainly at the left and right ES regions, respectively. If l_{SC} is not sufficiently large, the two degenerate bound states are well coupled and then split into two nondegenerate states. As shown in Fig. 2(c), the MBSs with $E/\Delta = 0$ split into two states with $E/\Delta = \pm 0.019$, the fermionic ABSs with $E/\Delta = 0.390$ split into two states with $E/\Delta = 0.370$ and 0.412, and the fermionic ABSs with $E/\Delta = 0.760$ split into two states with $E/\Delta = 0.737$ and 0.792. Compared with the uncoupled states in Fig. 2(b), we find that the maximum probability density ρ is halved when the bound states are coupled in Fig. 2(c). This sharp decrease in ρ indicates that the degenerate bound states are well coupled. Furthermore, the amplitude of coupling is nearly same because the probability densities ρ differ only slightly in Fig. 2(c). In brief, when the MBSs of the pair are coupled, the fermionic ABSs of each pair are finely coupled simultaneously, as illustrated in Figs. 2(b) and 2(c). Herein, we consider $\mu_{\mathrm{FI1}} = \mu_{\mathrm{FI2}} = 0$, $\mu_{\mathrm{ES1}} = \mu_{\mathrm{ES2}} = 10\Delta$, and $m_{lz} = m_{rz} = \Delta$.

Because the couplings of the MBSs and fermionic ABSs are considerably important, we extend the scope of the study to investigate the coupling properties of all pairs of degenerate bound states in Fig. 3. To ensure the formation of twofold-degenerate bound states, the widths of the ESs on either side of the SC are configured to be the same in Fig. 1(b). First, we plot the dependence of the energies of all bound states on the chemical potential μ_{SC} in Fig. 3(a). As μ_{SC} is increased, we find that the energies of the bound states of each pair

periodically oscillate with a constant amplitude. Figure 3(b) shows how the bound-state energies depend on the width l_{EG1}. We find that the energies of the bound states of each pair oscillate with an increase in l_{ES1}. Because the energies of the degenerate fermionic ABSs decrease with an increase in l_{ES1}, as shown in Fig. 2(a), the energies of the corresponding bound states of each pair decrease with an increase in l_{ES1} as a whole. Therefore, the coupling strength of the bound states of each pair decreases slightly and periodically with an increase in l_{ES1} overall in Fig. 3(b).

In Fig. 3, we see that the coupling strengths of all pairs of bound states display the same tendency with the increase of μ_{SC} or l_{ES1}. Concretely, the coupling strengths maximize/minimize in phase with each other. This property provides the physical picture to intuitively understand the transport properties discussed below.

IV. CURRENT-CURRENT CORRELATIONS (CCCs)

We study the transport properties of the MBSs and ordinary fermionic ABSs in the junction shown in Fig. 1(b). This can be realized by connecting the junction to two separate ES leads, whereupon the transport setup becomes the junction shown in Fig. 1(c). The chemical potentials of the left and the right leads are denoted by μ_{ESL} and μ_{ESR}, respectively. Based on the scattering matrix S in Appendix A, we can calculate the time-averaged current $\bar{I}_i$ and the current fluctuation $\delta I_i(t) = I_i(t) - \bar{I}_i$ in lead i. In our setup shown in Fig. 1(c), the left and right leads are equally biased at voltage V, whereas the middle SC is grounded. The Fano factor measures the charge transfer in a current pulse, which is defined by the ratio of the noise correlator P_{ij} to the mean current $\bar{I}_i$. The noise correlator P_{ij} is defined as $P_{ij} = \int_{-\infty}^{\infty} dt\, \overline{\delta I_i(0)\delta I_j(t)}$. According to the scattering matrix elements in Eq. (A5), the mean current and noise correlator can be calculated as follows [48]:

$$\bar{I}_i = \frac{e}{2\pi\hbar} \sum_{k\in 1,2;\beta,\gamma\in e,h} \mathrm{sgn}(\beta) \int_0^{\infty} dE\, A_{kk}^{\gamma\gamma}(i,\beta,E) f_{i,\beta}(E),$$

$$A_{kl}^{\gamma\delta}(i,\beta,E) = \delta_{ik}\delta_{il}\delta_{\beta\gamma}\delta_{\beta\delta} - \left(s_{ik}^{\beta\gamma}\right)^* s_{il}^{\beta\delta},$$

$$P_{ij} = \frac{e^2}{2\pi\hbar} \sum_{k,l\in 1,2;\beta,\gamma,\zeta,\eta\in e,h} \mathrm{sgn}(\beta)\mathrm{sgn}(\gamma) \int_0^{\infty} dE\, A_{kl}^{\zeta\eta}(i,\beta,E) \times A_{lk}^{\eta\zeta}(j,\gamma,E) f_{i,\beta}(E)[1 - f_{j,\gamma}(E)], \quad (8)$$

where i, j, k, and l denote the channels. For example, $k = 1$ and 2 indicate the two channels in the left and right leads, respectively. The electron (e) and hole (h) channels are denoted by β, γ, ζ, and η. Here, $\mathrm{sgn}(\beta) = 1$ for $\beta = e$ and $\mathrm{sgn}(\beta) = -1$ for $\beta = h$. The differential conductance in lead i is $G_i = d\bar{I}_i/dV$, and G_1 is equal to G_2 because the bias voltage V in the two leads is the same. The differential noise correlator is defined as $\mathcal{P}_{ij}(E) = dP_{ij}/d(eV)$. It is caused by electrons with energy E and measures the CCC between the leads i and j. To make the cross CCC sufficiently large, the left and right FIs are set to be adequately long to suppress the local Andreev reflection and enhance the crossed Andreev reflection in Fig. 1(c).

Figure 4(a) shows the current-current fluctuation correlators, which are calculated at zero temperature and represented

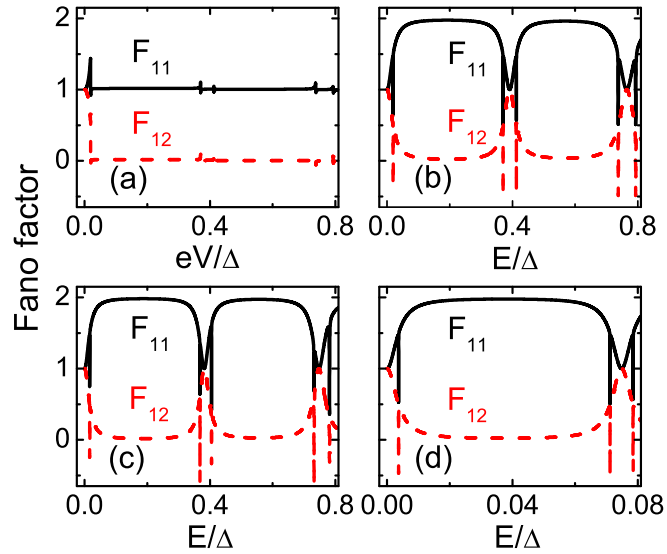

FIG. 4. (a) Fano factors of the junction as functions of bias voltage V. (b)–(d) Fano factors as functions of energy E of incident electrons. Here, $\mu_{\mathrm{ESL}} = \mu_{\mathrm{ESR}} = 10\Delta$, $\mu_{\mathrm{SC}} = 50\Delta$, $l_{\mathrm{SC}} = 2.5\xi$, and $l_{\mathrm{FI1}} = l_{\mathrm{FI2}} = 4\xi$. $l_{\mathrm{ES1}} = l_{\mathrm{ES2}} = 3\xi$ in (a) and (b), $l_{\mathrm{ES1}} = 3\xi$ and $l_{\mathrm{ES2}} = 3.1\xi$ in (c), and $l_{\mathrm{ES1}} = l_{\mathrm{ES2}} = 20\xi$ in (d).

by the Fano factors F_{11} and F_{12}. F_{11} denotes the autocorrelator P_{11}, which is normalized by $e\bar{I}_1$, and F_{12} denotes the cross correlator P_{12}, which is normalized by $e\bar{I}_1 = e\bar{I}_2 = e(\bar{I}_1 + \bar{I}_2)/2$. Figure 4(a) plots the dependence of F_{11} and F_{12} on the bias voltage V, and we observe that F_{11} and F_{12} are both equal to unity at $V/\Delta = 0$. $F_{11} = 1$ indicates that the current pulse in lead 1 transfers one electron into the SC, while $F_{12} = 1$ signifies both suppression of the local Andreev reflection and enhancement of the crossed Andreev reflection. As pointed out in previous research [40], for any stochastic process the cross correlator is bound by the autocorrelator with $|P_{12}| \leqslant (P_{11} + P_{22})/2$. At $V/\Delta = 0$, we have $P_{12} = (P_{11} + P_{22})/2 = P_{11}$ because $P_{11} = P_{22}$, making the cross correlator positive and maximally large for each current pulse. When V is away from zero, the Fano factors F_{11} and F_{12} are mainly equal to 1 and 0, respectively. Such signals imply that the current fluctuations in the two leads are independent. Note that for a given bias voltage (V), the current correlators and the mean currents are calculated by summing over all contributions from $E/\Delta = 0$ to eV. In Fig. 4(a), F_{11} and F_{12} show four small peaks at either side of $eV/\Delta = 0.39$ and 0.76. These peaks signify some unusual transport properties of ordinary fermionic ABSs.

In Fig. 4(b), we show the dependencies of the differential Fano factors F_{11} and F_{12} on the energy E of the incident electrons, where $F_{11}(E) = \mathcal{P}_{11}/G_1$ and $F_{12}(E) = \mathcal{P}_{12}/[(G_1 + G_2)/2] = \mathcal{P}_{12}/G_1$ because $G_1 = G_2$. We can observe that $F_{11} = F_{12}$ at three energy points, namely, $E/\Delta = 0$, 0.39, and 0.76. As pointed out in the aforementioned section, $E/\Delta = 0$ corresponds to the MBS energy, whereas $E/\Delta = 0.39$ and 0.76 correspond to the energies of the two different fermionic ABSs. Therefore, the fluctuations of the currents flowing from the two leads into the SC are maximally correlated at the energies of the MBSs and fermionic ABSs. This considerably

differs from previous work [46,47] in which MBS signatures in CCCs were distinct from those of fermionic ABSs. This difference is clarified right now. According to the Altland-Zirnbauer topological classification [49], the symmetry class of the Hamiltonian of our superconducting system is D class. When the MBSs are tunnel coupled, the fermionic ABSs of each pair are tunnel coupled likewise, as illustrated by Figs. 2(b) and 2(c). Since the coupling strengths of all pairs of bound state maximize/minimize in phase with each other as shown in Fig. 3, maximal cross CCCs induced by MBSs and ABSs appear simultaneously. Therefore, cross CCCs can be induced by both kinds of states, then are universal for both kinds of states in our setup. In Refs. [46] and [47], the superconducting nanowire and superconducting chain of magnetic atoms belong to D class in general. In these two superconducting systems, two MBSs are tunnel coupled, while the fermionic ABSs are not tunnel coupled. Hence, MBSs can induce cross CCC, while the fermionic ABSs cannot in Refs. [46,47].

When the energy E is away from those of the three bound states in Fig. 4(b), F_{11} reaches 2 and F_{12} reaches 0, thereby demonstrating that only local Andreev reflection occurs in those regions. On comparing Figs. 4(a) and 4(b), we find that the Fano factors show the same characteristics near $V/\Delta = 0$ and $E/\Delta = 0$. This type of characteristics is attributed to the weak integral effect over the energy from $E/\Delta = 0$ to $E/\Delta = eV$ when the bias voltage is small. Therefore, the manner in which F_{11} and F_{12} depend on energy E can well reveal the properties of the CCCs induced by the MBSs and fermionic ABSs.

Next, we study the influence of the structural asymmetry on the CCCs. The structural asymmetry can be different l_{ES1} and l_{ES2}, different μ_{ES1} and μ_{ES2}, different l_{FI1} and l_{FI2}, different μ_{FI1} and μ_{FI2}, or different μ_{ESL} and μ_{ESR}. It is found that CCCs induced by the MBSs and fermionic ABSs are unaffected by these asymmetries. An example is given in Fig. 4(c), which shows the dependencies of the Fano factors on energy E, where $l_{\mathrm{ES1}} = 3\xi$ and $l_{\mathrm{ES2}} = 3.1\xi$. Since ξ is quite long as given below, $l_{\mathrm{ES1}} = 3\xi$ and $l_{\mathrm{ES2}} = 3.1\xi$ mean the structure of system is quite asymmetric. Such correlations always appear, provided that the asymmetry between l_{ES1} and l_{ES2} does not strongly break the coupling of the two corresponding bound states. The coupling of the two corresponding bound states is clearly shown in Fig. 5 in Appendix B. Therefore, the CCCs are robust to the asymmetry of the system's structure in our setup. Furthermore, we consider the transport properties of the fermionic ABSs of a pair when their energies are considerably close to the energies of the MBSs of the pair. According to Fig. 2(a), we know that fermionic ABSs with considerably low energies will appear when l_{ES1} and l_{ES2} are sufficiently large. Figure 4(d) plots the dependencies of the Fano factors on energy E, where the energies of the fermionic ABSs are close to the MBS energy and the cross CCCs induced by the MBSs and fermionic ABSs are both maximal.

Finally, we discuss the experimental realization of our setup in Fig. 1. The 2D topological insulators (2D TIs) have been realized in HgTe/CdTe quantum wells, InAs/GaSb quantum wells, and monolayer WTe_2. The bulk gaps for these three kinds of materials are about 10 meV [50], 4 meV [51], and 100 meV [52], respectively. The superconducting energy gap of the ESs could be induced by depositing the superconductor on the edge of a 2D TI. The induced superconducting energy gaps are about 0.023 meV for HgTe/CdTe quantum well [53] and 0.12 meV for InAs/GaSb quantum well [54]. Thus, the superconducting coherence length ξ are about 400 to 2400 nm for $\upsilon_{\mathrm{F}} \simeq 10^5$ m/s [50,51,55]. Proximity-effect-induced ferromagnetism on the surface states of three-dimensional TIs have been realized in experiments [56]. Induced ferromagnetisms by EuS, YIG, and monolayer CrI_3 have been observed [56,57]; these findings lay the groundwork for realizing the proximity-induced ferromagnetism in 2D TIs. Thus at present, the parameters and results in our work can be accessible in real life systems. We suggest that HgTe/CdTe quantum well and monolayer WTe_2 are good candidate TIs for the exploration of the physics in our setup.

V. CONCLUSIONS

We studied the MBSs and ordinary fermionic ABSs in a 2D TI system. Our findings reveal that the coupling strengths of both MBSs and ordinary fermionic ABSs depend on the system parameters in the same pattern. These two types of bound states can lead to the same differential CCCs, and such CCCs are robust to the asymmetry of the system's structure. These characteristics demonstrate a universal property in 2D TI systems. In order to certainly distinguish MBSs from fermionic ABSs in 2D TI systems, it is crucial to have characteristics beyond the CCCs.

ACKNOWLEDGMENTS

We acknowledge discussions with W.-K. Tse and X. Liu. This work was financially supported by the National Key Research and Development Program (Grants No. 2017YFB0405703 and No. 2016YFA0301700), the National Natural Science Foundation of China (Grants No. 11474265 and No. 11704366), China Postdoctoral Science Foundation (Grant No. 2016M590569), the Fundamental Research Funds for the Central Universities (Grant No. WK2340000087), and the China Government Youth 1000-Plan Talent Program. We are grateful to the supercomputing service of AM-HPC and the Supercomputing Center of USTC for providing the high-performance computing resources.

APPENDIX A: SCATTERING MATRIX

By solving Eq. (1), we can obtain the wave functions for the junction in Fig. 1(c). For an incident electron wave function in the left ES lead, the wave function in the left ES lead is

$$\begin{aligned}\psi_{\mathrm{ESL}} = & \frac{1}{\sqrt{(E+\mu_{\mathrm{ESL}})\hbar\upsilon_{\mathrm{F}}k_{\mathrm{ESL}}}}\psi^{e}_{\mathrm{ESL}}\exp(ik_{\mathrm{ESL}}x) \\ & + s^{ee}_{11}\frac{1}{\sqrt{(E+\mu_{\mathrm{ESL}})\hbar\upsilon_{\mathrm{F}}k_{\mathrm{ESL}}}}\psi^{e'}_{\mathrm{ESL}}\exp(-ik_{\mathrm{ESL}}x) \\ & + s^{he}_{11}\frac{1}{\sqrt{|(E-\mu_{\mathrm{ESL}})\hbar\upsilon_{\mathrm{F}}k'_{\mathrm{ESL}}|}}\psi^{h}_{\mathrm{ESL}}\exp(ik'_{\mathrm{ESL}}x),\end{aligned} \tag{A1}$$

where s_{11}^{ee}, s_{11}^{he} are the coefficients of wave functions for reflected electron and local Andreev reflected hole, respectively. $\psi_{\rm ESL}^{e} = (\hbar\upsilon_{\rm F}k_{\rm ESL}, E + \mu_{\rm ESL}, 0, 0)^T$, $\psi_{\rm ESL}^{e'} = (-\hbar\upsilon_{\rm F}k_{\rm ESL}, E + \mu_{\rm ESL}, 0, 0)^T$, and $\psi_{\rm ESL}^{h} = (0, 0, -\hbar\upsilon_{\rm F}k_{\rm ESL}, E - \mu_{\rm ESL})^T$. Here, $k_{\rm ESL} = (\mu_{\rm ESL} + E)/\hbar\upsilon_{\rm F}$ and $k_{\rm ESL} = (\mu_{\rm ESL} - E)/\hbar\upsilon_{\rm F}$.

The wave function in the left FI is

$$\psi_{\rm FI1} = a_e\psi_{\rm FI1}^{e}\exp\left[-i\left(k_l + \frac{2m_{lx}}{\hbar\upsilon_{\rm F}}\right)x\right] + a_e'\psi_{\rm FI1}^{e'}\exp[ik_l x] + a_h\psi_{\rm FI1}^{h}\exp\left[i\left(\frac{2m_{lx}}{\hbar\upsilon_{\rm F}} - k_l'\right)x\right] + a_h'\psi_{\rm FI1}^{h'}\exp[ik_l' x], \tag{A2}$$

where $\psi_{\rm FI1}^{e} = (-\hbar\upsilon_{\rm F}k_l - m_{lx} - im_{ly}, E + \mu_{\rm FI1} - m_{lz}, 0, 0)^T$, $\psi_{\rm FI1}^{e'} = (\hbar\upsilon_{\rm F}k_l + m_{lx} - im_{ly}, E + \mu_{\rm FI1} - m_{lz}, 0, 0)^T$, $\psi_{\rm FI1}^{h} = (0, 0, \hbar\upsilon_{\rm F}k_l' - m_{lx} - im_{ly}, E - \mu_{\rm FI1} - m_{lz})^T$, and $\psi_{\rm FI1}^{h'} = (0, 0, -\hbar\upsilon_{\rm F}k_l' + m_{lx} - im_{ly}, E - \mu_{\rm FI1} - m_{lz})^T$. $k_l = (i\sqrt{-(E + \mu_{\rm FI1})^2 + m_{lz}^2 + m_{ly}^2} - m_{lx})/\hbar\upsilon_{\rm F}$ and $k_l' = (i\sqrt{-(E - \mu_{\rm FI1})^2 + m_{lz}^2 + m_{ly}^2} + m_{lx})/\hbar\upsilon_{\rm F}$. a_e a_e', a_h, and a_h' are the coefficients of wave functions.

The wave functions of the left ES, middle SC, and right ES in Fig. 1(c) are $\psi_{\rm ES1}$, $\psi_{\rm SC}$,and $\psi_{\rm ES2}$, respectively, which are the same as those in Fig. 1(b). The wave function in the right FI is

$$\psi_{\rm FI2} = q_e'\psi_{\rm FI2}^{e'}\exp\left[-i\left(k_r + \frac{2m_{rx}}{\hbar\upsilon_{\rm F}}\right)x\right] + q_e\psi_{\rm FI2}^{e}\exp[ik_r x] + q_h'\psi_{\rm FI2}^{h'}\exp\left[i\left(\frac{2m_{rx}}{\hbar\upsilon_{\rm F}} - k_r'\right)x\right] + q_h\psi_{\rm FI2}^{h}\exp[ik_r' x], \tag{A3}$$

where $\psi_{\rm FI2}^{e'} = (-\hbar\upsilon_{\rm F}k_r - m_{rx} - im_{ry}, E + \mu_{\rm FI2} - m_{rz}, 0, 0)^T$, $\psi_{\rm FI2}^{e} = (\hbar\upsilon_{\rm F}k_r + m_{rx} - im_{ry}, E + \mu_{\rm FI2} - m_{rz}, 0, 0)^T$, $\psi_{\rm FI2}^{h'} = (0, 0, \hbar\upsilon_{\rm F}k_r' - m_{rx} - im_{ry}, E - \mu_{\rm FI2} - m_{rz})^T$, and $\psi_{\rm FI2}^{h} = (0, 0, -\hbar\upsilon_{\rm F}k_r' + m_{rx} - im_{ry}, E - \mu_{\rm FI2} - m_{rz})^T$. $k_r = (i\sqrt{-(E + \mu_{\rm FI2})^2 + m_{rz}^2 + m_{ry}^2} - m_{rx})/\hbar\upsilon_{\rm F}$ and $k_r' = (i\sqrt{-(E - \mu_{\rm FI2})^2 + m_{rz}^2 + m_{ry}^2} + m_{rx})/\hbar\upsilon_{\rm F}$. q_e q_e', q_h, and q_h' are the coefficients of wave functions.

The wave function in the right ES lead is

$$\psi_{\rm ESR} = s_{21}^{ee}\frac{1}{\sqrt{(E + \mu_{\rm ESR})\hbar\upsilon_{\rm F}k_{\rm ESR}}}\psi_{\rm ESR}^{e}\exp(ik_{\rm ESR}x) + s_{21}^{he}\frac{1}{\sqrt{|(E - \mu_{\rm ESR})\hbar\upsilon_{\rm F}k_{\rm ESR}'|}}\psi_{\rm ESR}^{h}\exp(ik_{\rm ESR}'x), \tag{A4}$$

where s_{21}^{ee}, s_{21}^{he} are the coefficients of wave functions for tunneling electron and crossed Andreev reflected hole, respectively. $\psi_{\rm ESR}^{e} = (\hbar\upsilon_{\rm F}k_{\rm ESR}, E + \mu_{\rm ESR}, 0, 0)^T$ and $\psi_{\rm ESR}^{h} = (0, 0, -\hbar\upsilon_{\rm F}k_{\rm ESR}, E - \mu_{\rm ESR})^T$. Here, $k_{\rm ESR} = (\mu_{\rm ESR} + E)/\hbar\upsilon_{\rm F}$ and $k_{\rm ESR}' = -(\mu_{\rm ESR} - E)/\hbar\upsilon_{\rm F}$.

The wave functions in different regions satisfy continuity conditions at the interfaces $\psi_{\rm ESL}(x = -l_{\rm FI1} - l_{\rm ES1}) = \psi_{\rm FI1}(x = -l_{\rm FI1} - l_{\rm ES1})$, $\psi_{\rm FI1}(x = -l_{\rm ES1}) = \psi_{\rm ES1}$ $(x = -l_{\rm ES1})$, $\psi_{\rm ES1}(x = 0) = \psi_{\rm SC}(x = 0)$, $\psi_{\rm SC}(x = l_{\rm SC}) = \psi_{\rm ES2}(x = l_{\rm SC})$, $\psi_{\rm ES2}(x = l_{\rm SC} + l_{\rm ES2}) = \psi_{\rm FI2}(x = l_{\rm SC} + l_{\rm ES2})$, and $\psi_{\rm FI2}(x = l_{\rm SC} + l_{\rm ES2} + l_{\rm FI2}) = \psi_{\rm ESR}(x = l_{\rm SC} + l_{\rm ES2} + l_{\rm FI2})$, which determine the coefficients s_{11}^{ee}, s_{11}^{he}, s_{21}^{ee}, and s_{21}^{he}.

With the same method, for an incident hole wave function in the left ES lead, the wave functions in different regions satisfy continuity conditions at the interfaces, which determine the coefficients s_{11}^{eh}, s_{11}^{hh}, s_{21}^{eh}, and s_{21}^{hh}. For an incident elecron wave function in the right ES lead, the wave functions in different regions satisfy continuity conditions at the interfaces, which determine the coefficients s_{12}^{ee}, s_{12}^{he}, s_{22}^{ee}, and s_{22}^{he}. For an incident hole wave function in the right ES lead, the wave functions in different regions satisfy continuity conditions at the interfaces, which determine the coefficients s_{12}^{eh}, s_{12}^{hh}, s_{22}^{eh}, and s_{22}^{hh}.

Thus, for the setup in Fig. 1(c), the scattering matrix S is given with the following form:

$$S = \begin{pmatrix} s_{11}^{ee} & s_{12}^{ee} & s_{11}^{eh} & s_{12}^{eh} \\ s_{21}^{ee} & s_{22}^{ee} & s_{21}^{eh} & s_{22}^{eh} \\ s_{11}^{he} & s_{12}^{he} & s_{11}^{hh} & s_{12}^{hh} \\ s_{21}^{he} & s_{22}^{he} & s_{21}^{hh} & s_{22}^{hh} \end{pmatrix}. \tag{A5}$$

APPENDIX B: MBSs AND FERMIONIC ABSs IN THE ASYMMETRICAL FI–ES–SC–ES–FI JUNCTION

In the main text, we have shown the energies of Majorana bound state (MBS) and fermionic Andreev bound states (ABSs) as a function of the width $l_{\rm ES1}$ in a FI–ES–SC junction in Fig. 2(a). Also, we have shown the probability densities of the MBS and ABSs in Fig. 2(b) for $l_{\rm ES1} = 3.0\xi$, the energies E/Δ of MBS, first ABS, and second ABS are 0, 0.39, and 0.76, respectively. Note that we only discuss the bound states with zero and positive energies for conciseness in the main text and in this Appendix, the probability densities of the negative-energy ABSs are the same as those of the corresponding positive-energy ABSs. All the energies of bound states are rounded off to three significant digits. In a symmetrical FI–ES–SC–ES–FI junction with $l_{\rm ES1} = l_{\rm ES2} = 3\xi$ and $l_{\rm SC} = 2.5\xi$, there are two degenerate bound states for every above obtained energy, and the degenerate bound states of every pair are well coupled and split into two nondegenerate states. The energies and probability densities of the nondegenerate states have been shown in Fig. 2(c). By comparing the energies of the uncoupled and the coupled bound states of every pair, we find the coupling strengths (or splitting amplitudes) of the bound states of all pairs are different and dependent on the energies of the degenerate bound states. Our result is better than the less rigorous conclusion in Ref. [58], which is as follows: "*The splitting of cavity levels by hybridization is always the same, independently of which parameters are used.*"

In order to clearly study the coupling strengths of the bound states in the asymmetrical FI–ES–SC–ES–FI junction, first, we consider a FI–ES–SC–ES–FI junction with $l_{\rm ES1} = 3\xi$, $l_{\rm ES2} = 3.1\xi$, and $l_{\rm SC} = 2.5\xi$. The energies of MBS and ABSs in the SC–ES–FI junction with the width $l_{\rm ES2} = 3.1\xi$ can be given according to the known result of the FI–ES–SC junction in Fig. 2(a), and the energies E/Δ of MBS, first ABS, and second ABS are 0, 0.381, and 0.743, respectively. The

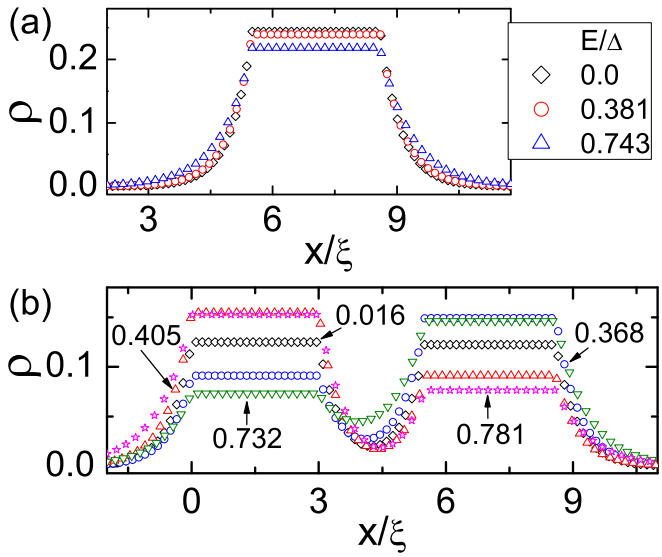

FIG. 5. (a) Probability densities ρ of MBS and fermionic ABSs as functions of x in the SC–ES–FI junction, where $x = 5.5\xi$ is the interface between the left SC and middle ES, and the ES width is $l_{ES2} = 3.1\xi$. (b) Probability densities ρ of coupled MBSs and coupled fermionic ABSs as functions of x in the asymmetrical FI–ES–SC–ES–FI juncton, where $x = 0$ is the interface between the leftmost FI and left ES, $l_{SC} = 2.5\xi$, $l_{ES1} = 3\xi$, and $l_{ES2} = 3.1\xi$. Here, the chemical potential $\mu_{SC} = 50\Delta$, and $\xi = \hbar v_F/\Delta$ is the coherence length.

probability densities of these three bound states in this SC–ES–FI junction are shown in Fig. 5(a); it is found that the maximal probability densities are in the range $5.5\xi < x < 8.6\xi$, three bound states are localized mainly in the ES region, and the MBS is slightly more localized than the ABSs. With the knowledge of the energies and probability densities of MBS and ABSs in the FI–ES–SC junction with $l_{ES1} = 3\xi$ and in the SC–ES–FI junction with $l_{ES1} = 3.1\xi$, we can easily give the coupling strengths of these bound states in the asymmetrical FI–ES–SC–ES–FI junction with $l_{ES1} = 3\xi$, $l_{ES2} = 3.1\xi$, and $l_{SC} = 2.5\xi$. The energies and the corresponding probability densities of the bound states in this asymmetrical FI–ES–SC–ES–FI junction are given in Fig. 5(b), we can see that the coupling energy E/Δ of MBSs is 0.016, which is different from that in the symmetrical junction with $l_{ES1} = l_{ES2} = 3\xi$, and $l_{SC} = 2.5\xi$. Even though the ABS with $E/\Delta = 0.390$ and the ABS with $E/\Delta = 0.381$ have different energies, these two ABSs are coupled and becoming two new ABSs with $E/\Delta = 0.405$ and $E/\Delta = 0.368$, respectively. The same for the ABS with $E/\Delta = 0.760$ and the ABS with $E/\Delta = 0.743$, they are coupled and becoming two new ABSs with $E/\Delta = 0.781$ and $E/\Delta = 0.732$, respectively.

Second, we further consider an asymmetrical FI–ES–SC–ES–FI junction with $l_{ES1} = 3\xi$, $l_{ES2} = 5\xi$, and $l_{SC} = 2.5\xi$. The energies of MBS and ABSs in the SC–ES–FI junction with $l_{ES2} = 5\xi$ also can be given according to the known result of the FI–ES–SC junction in Fig. 2(a), the energies E/Δ of MBS, first ABS, second ABS, third ABS, and fourth ABS are 0, 0.2613 [rounded off to four significant digits], 0.519, 0.767, and 0.981, respectively. The energies E/Δ of bound states in this asymmetrical FI–ES–SC–ES–FI junction with $l_{ES1} = 3\xi$, $l_{ES2} = 5\xi$, and $l_{SC} = 2.5\xi$ are 0.012, 0.2609 [rounded off to four significant digits], 0.391, 0.521, 0.750, 0.785, and 0.990, respectively. We can know that the coupling energy E/Δ of MBSs is 0.012, and the ABSs with $E/\Delta = 0.760$ and $E/\Delta = 0.767$ are well coupled and becoming two new ABSs with $E/\Delta = 0.750$ and $E/\Delta = 0.785$, respectively. The ABS, whose energy E/Δ is 0.2613, becomes a new state with energy E/Δ is 0.2609. Thus, this state with energy E/Δ is 0.2613 and is approximately independent of the other bound sates, so are the ABSs, whose energies E/Δ are 0.390, 0.519, and 0.990, respectively. The coupling strengths of all these states can also be understood from the changes of their probability densities when l_{SC} changes from infinite to 2.5ξ. The probability densities of all these states, like those have been given in Figs. 2(b) and 2(c), and Fig. 5, are also calculated, but not shown by detailed figures here.

As a result, in an asymmetrical FI–ES–SC–ES–FI junction, although the number of the bound states on the left FI–ES–SC side is different from that on the right SC–ES–FI side, two bound states on the left and right sides can also be well coupled so long as their energies are slightly different. Our result is better than the less rigorous conclusion in Ref. [58], which is as follows: "*For the asymmetric double cavity ($d_{NL} \neq d_{NR}$), the number of ABSs on each cavity can be different. In that case, the levels do not hybridize.*"

[1] F. Wilczek, Nat. Phys. **5**, 614 (2009).
[2] S. R. Elliott and M. Franz, Rev. Mod. Phys. **87**, 137 (2015); R. Aguado, La Rivista del Nuovo Cimento **40**, 523 (2017).
[3] A. Y. Kitaev, Phys. Usp. **44**, 131 (2001).
[4] D. A. Ivanov, Phys. Rev. Lett. **86**, 268 (2001).
[5] C. Nayak, S. H. Simon, A. Stern, M. Freedman, and S. Das Sarma, Rev. Mod. Phys. **80**, 1083 (2008).
[6] A. Y. Kitaev, Ann. Phys. (NY) **303**, 2 (2003).
[7] G. Moore and N. Read, Nucl. Phys. B **360**, 362 (1991); N. Read and D. Green, Phys. Rev. B **61**, 10267 (2000).
[8] S. Das Sarma, C. Nayak, and S. Tewari, Phys. Rev. B **73**, 220502(R) (2006).
[9] S. Tewari, S. Das Sarma, C. Nayak, C. Zhang, and P. Zoller, Phys. Rev. Lett. **98**, 010506 (2007).
[10] L. Fu and C. L. Kane, Phys. Rev. Lett. **100**, 096407 (2008).
[11] L. Fu and C.L. Kane, Phys. Rev. B **79**, 161408(R) (2009).
[12] J. D. Sau, R. M. Lutchyn, S. Tewari, and S. Das Sarma, Phys. Rev. Lett. **104**, 040502 (2010).
[13] J. Alicea, Phys. Rev. B **81**, 125318 (2010).
[14] R. M. Lutchyn, J. D. Sau, and S. Das Sarma, Phys. Rev. Lett. **105**, 077001 (2010).
[15] Y. Oreg, G. Refael, and F. von Oppen, Phys. Rev. Lett. **105**, 177002 (2010).

[16] S. Nadj-Perge, I. K. Drozdov, B. A. Bernevig, and A. Yazdani, Phys. Rev. B **88**, 020407(R) (2013).

[17] K. Sengupta, I. Žutić, H. J. Kwon, V. M. Yakovenko, and S. Das Sarma, Phys. Rev. B **63**, 144531 (2001).

[18] K. T. Law, P. A. Lee, and T. K. Ng, Phys. Rev. Lett. **103**, 237001 (2009).

[19] L. Fu and C. L. Kane, Phys. Rev. Lett. **102**, 216403 (2009); A. R. Akhmerov, J. Nilsson, and C. W. J. Beenakker, *ibid.* **102**, 216404 (2009).

[20] Y. Tanaka, T. Yokoyama, and N. Nagaosa, Phys. Rev. Lett. **103**, 107002 (2009); J. Linder, Y. Tanaka, T. Yokoyama, A. Sudbø, and N. Nagaosa, *ibid.* **104**, 067001 (2010).

[21] K. Flensberg, Phys. Rev. B **82**, 180516(R) (2010); C. Benjamin and J. K. Pachos, *ibid.* **81**, 085101 (2010).

[22] S. Das Sarma, J. D. Sau, and T. D. Stanescu, Phys. Rev. B **86**, 220506(R) (2012).

[23] J. J. He, T. K. Ng, P. A. Lee, and K. T. Law, Phys. Rev. Lett. **112**, 037001 (2014).

[24] J. J. He, J. Wu, T. P. Choy, X. J. Liu, Y. Tanaka, and K. T. Law, Nat. Commun. **5**, 3232 (2014).

[25] M. Trif and P. Simon, Phys. Rev. B **92**, 014503 (2015); P. Devillard, D. Chevallier, and M. Albert, *ibid.* **96**, 115413 (2017); C. Fleckenstein, N. T. Ziani, and B. Trauzettel, *ibid.* **97**, 134523 (2018).

[26] L. P. Rokhinson, X. Liu, and J. K. Furdyna, Nat. Phys. **8**, 795 (2012).

[27] V. Mourik, K. Zuo, S. Frolov, S. Plissard, E. Bakkers, and L. Kouwenhoven, Science **336**, 1003 (2012).

[28] M. T. Deng, C. L. Yu, G. Y. Huang, M. Larsson, P. Caroff, and H. Q. Xu, Nano Lett. **12**, 6414 (2012).

[29] H. H. Sun, K. W. Zhang, L. H. Hu, C. Li, G. Y. Wang, H. Y. Ma, Z. A. Xu, C. L. Gao, D. D. Guan, Y. Y. Li, C. Liu, D. Qian, Y. Zhou, L. Fu, S. C. Li, F. C. Zhang, and J. F. Jia, Phys. Rev. Lett. **116**, 257003 (2016).

[30] S. Nadj-Perge, I. K. Drozdov, J. Li, H. Chen, S. Jeon, J. Seo, A. H. MacDonald, B. A. Bernevig, and A. Yazdani, Science **346**, 602 (2014).

[31] Q. L. He, L. Pan, A. L. Stern, E. Burks, X. Che, G. Yin, J. Wang, B. Lian, Q. Zhou, E. S. Choi, K. Murata, X. Kou, T. Nie, Q. Shao, Y. Fan, S.-C. Zhang, K. Liu, J. Xia, and K. L. Wang, Science **357**, 294 (2017).

[32] H. Zhang, C. X. Liu, S. Gazibegovic, D. Xu, J. Logan, G. Wang, N. van Loo, J. Bommer, M. de Moor, D. Car, R. Op het Veld, P. van Veldhoven, S. Koelling, M. Verheijen, M. Pendharkar, D. Pennachio, B. Shojaei, J. Lee, C. Palmstrom, E. Bakkers *et al.*, Nature (London) **556**, 74 (2018).

[33] J. Liu, A. C. Potter, K. T. Law, and P. A. Lee, Phys. Rev. Lett. **109**, 267002 (2012).

[34] D. Pikulin, J. Dahlhaus, M. Wimmer, H. Schomerus, and C. Beenakker, New J. Phys. **14**, 125011 (2012).

[35] E. Prada, P. San-Jose, and R. Aguado, Phys. Rev. B **86**, 180503(R) (2012).

[36] E. J. H. Lee, X. Jiang, R. Aguado, G. Katsaros, C. M. Lieber, and S. De Franceschi, Phys. Rev. Lett. **109**, 186802 (2012).

[37] W. Ji and X. G. Wen, Phys. Rev. Lett. **120**, 107002 (2018).

[38] Y. H. Li, J. Liu, H. Liu, H. Jiang, Q. F. Sun, and X. C. Xie, Phys. Rev. B **98**, 045141 (2018).

[39] C. J. Bolech and E. Demler, Phys. Rev. Lett. **98**, 237002 (2007).

[40] J. Nilsson, A. R. Akhmerov, and C. W. J. Beenakker, Phys. Rev. Lett. **101**, 120403 (2008).

[41] L. Fu, Phys. Rev. Lett. **104**, 056402 (2010).

[42] C. W. J. Beenakker, Annu. Rev. Condens. Matter Phys. **4**, 113 (2013).

[43] S. M. Albrecht, A. P. Higginbotham, M. Madsen, F. Kuemmeth, T. S. Jespersen, J. Nygård, P. Krogstrup, and C. M. Marcus, Nature (London) **531**, 206 (2016).

[44] A. F. Andreev, Zh. Eksp. Teor. Fiz. **46**, 1823 (1964) [Sov. Phys. –JETP **19**, 1228 (1964)].

[45] J. M. Byers and M. E. Flatte, Phys. Rev. Lett. **74**, 306 (1995).

[46] J. Liu, F. C. Zhang, and K. T. Law, Phys. Rev. B **88**, 064509 (2013).

[47] Y. M. Wu and X. J. Liu, arXiv:1511.08773.

[48] M. P. Anantram and S. Datta, Phys. Rev. B **53**, 16390 (1996).

[49] A. P. Schnyder, S. Ryu, A. Furusaki, and A. W. W. Ludwig, Phys. Rev. B **78**, 195125 (2008).

[50] M. König, S. Wiedmann, C. Brüne, A. Roth, H. Buhmann, L. W. Molenkamp, X. L. Qi, and S. C. Zhang, Science **318**, 766 (2007).

[51] I. Knez, R. R. Du, and G. Sullivan, Phys. Rev. Lett. **107**, 136603 (2011).

[52] S. Wu, V. Fatemi, Q. D. Gibson, K. Watanabe, T. Taniguchi, R. J. Cava, and P. Jarillo-Herrero1, Science **359**, 76 (2018).

[53] S. Hart, H. Ren, T. Wagner, P. Leubner, M. Mühlbauer, C. Brüne, H. Buhmann, L. W. Molenkamp, and A. Yacoby, Nat. Phys. **10**, 638 (2014).

[54] V. S. Pribiag, A. J. A. Beukman, F. Qu, M. C. Cassidy, C. Charpentier, W. Wegscheider, and L. P. Kouwenhoven, Nat. Nanotechnol. **10**, 593 (2015).

[55] X. Qian, J. Liu, L. Fu, and J. Li, Science **346**, 1344 (2014).

[56] C. Lee, F. Katmis, P. Jarillo-Herrero, J. S. Moodera, and N. Gedik, Nat. Commun. **7**, 12014 (2016); T. Hirahara, S. V. Eremeev, T. Shirasawa, Y. Okuyama, T. Kubo, R. Nakanishi, R. Akiyama, A. Takayama, T. Hajiri, S. Ideta, M. Matsunami, K. Sumida, K. Miyamoto, Y. Takagi, K. Tanaka, T. Okuda, T. Yokoyama, S. Kimura, S. Hasegawa, and E. V. Chulkov, Nano Lett. **17**, 3493 (2017).

[57] B. Huang, G. Clark, E. Navarro-Moratalla, D. R. Klein, R. Cheng, K. L. Seyler, D. Zhong, E. Schmidgall, M. A. McGuire, D. H. Cobden, W. Yao, D. Xiao, P. Jarillo-Herrero, and X. Xu, Nature (London) **546**, 270 (2017); P. Wei, S. Lee, F. Lemaitre, L. Pinel, D. Cutaia, W. Cha, F. Katmis, Y. Zhu, D. Heiman, J. Hone, J. S. Moodera, and C. T. Chen, Nat. Mater. **15**, 711 (2016); S. Singh, J. Katoch, T. Zhu, K. Y. Meng, T. Liu, J. T. Brangham, F. Yang, M. E. Flatté, and R. K. Kawakami, Phys. Rev. Lett. **118**, 187201 (2017).

[58] F. Keidel, P. Burset, and B. Trauzettel, Phys. Rev. B **97**, 075408 (2018).